JOURNAL OF PROPULSION AND POWER
Vol. 27, No. 4, July–August 2011

Hall-Effect Thruster–Cathode Coupling, Part II: Ion Beam and Near-Field Plume

Jason D. Sommerville* and Lyon B. King†
Michigan Technological University, Houghton, Michigan 49931

DOI: 10.2514/1.50124

This is the second part of a two-part paper in which the effect of cathode position and magnetic field configuration on Hall-effect thruster performance is explored. The effect magnetic field topology has on the coupling between a Hall-effect thruster and its cathode has been studied. With two Hall-effect thruster configurations, each with a different external field topology, the cathode is positioned across a range of radial distances and the effect on performance, ion beam, and near-field plasma is investigated. The importance of the magnetic field separatrix, a surface which divides the magnetic field lines into "internal" and "external" regions, is shown. In particular, total efficiency improvements of up to seven percentage points are seen when placing the cathode near the separatrix as opposed to locations further away of the thruster. Analysis of the thruster telemetry, ion beam current distribution, and ion energy distribution functions properties show the effect of the cathode position on the efficiency loss mechanisms of beam divergence, current utilization, ion velocity distribution, voltage utilization, and cathode coupling. Measurements of near-field plasma potential, electron temperature, and electron density provide help to explain why these efficiency improvements come about and add insight into the cathode coupling processes. As the cathode is moved radially away from the thruster up to 250 mm, the cathode coupling efficiency decreases by up to 10 percentage points. Furthermore, the near-field plasma potential increases by up to 30 V, and this is correlated with a decrease in beam divergence efficiency of up to 15 percentage points.

Nomenclature

A	=	probe area
D_{probe}	=	diameter of the Faraday probe electrode
f	=	ion energy distribution function
I	=	Langmuir probe current
I_{probe}	=	current measured by Faraday probe
$I_{i,\text{sat}}$	=	ion saturation current
j	=	ion beam current density
k	=	Boltzmann constant
m_e	=	electron mass
m_i	=	ion mass
n_e	=	electron density
r	=	radial position relative to the thruster axis; negative values are on the side opposite the cathode
r_p	=	probe radius
T_e	=	electron temperature
T_i	=	ion temperature
V	=	voltage applied to probe
V_{cg}	=	cathode coupling voltage
V_f	=	floating potential
V_p	=	plasma potential
v	=	ion velocity
$\langle x \rangle$	=	expectation (average) value of any quantity x
z	=	axial position relative to the exit plane of the thruster
α, β	=	empirical values for Peterson and Talbot probe analysis
η_θ	=	beam divergence efficiency
η_I	=	current utilization efficiency
η_V	=	voltage utilization efficiency
η_{Vcg}	=	cathode coupling efficiency
η_{vdf}	=	velocity distribution efficiency
λ_d	=	debye length
χ	=	nondimensional potential $\frac{eV}{kT_e}$, with respect to plasma potential
ψ	=	nondimensional applied probe potential
ψ_n	=	nondimensional potential of probe n with respect to floating potential

Presented as Paper 2009-5005 at the 45th AIAA/ASME/SAE/ASEE Joint Propulsion Conference & Exhibit, Denver, CO, 2–5 August 2009; received 31 March 2010; revision received 19 January 2011; accepted for publication 1 February 2011.

*Currently Chief Technologist, Aerophysics, Inc., 1402 E. Sharon Ave., Ste. 206. Student Member AIAA.

†Associate Professor, Dept. of Mechanical Engineering, Engineering Mechanics, 815 R. L. Smith Bldg., 1400 Townsend Dr. Member AIAA.

I. Introduction

IN THIS second paper, we focus on the changes in ion beam and near-field plume properties resulting from changing the cathode position with respect to the thruster. From analysis of the ion beam current distribution, ion energy distribution function (IEDF), we derive the efficiency loss mechanisms of beam divergence, voltage utilization, current utilization, and ion velocity distribution. Furthermore, we consider the cathode coupling efficiency, which is derived from the cathode coupling voltage. We show how these efficiency loss mechanisms change as the cathode is repositioned. Studying the near-field plume plasma potential, electron temperature and electron density gives us some insight into how the plasma structure changes in response to the cathode position and how that affects the efficiency of the thruster.

As discussed in the introduction of Part I [1], there have been numerous studies that looked at the performance of Hall-effect thrusters (HETs) versus cathode position and other cathode parameters. However, only a few of those studies have also incorporated any sort of ion beam or plume diagnostics. Most notably, work by Hofer et al. and Jameson et al. [2,3] comparing cathodes mounted internally and coaxially to the thruster versus those mounted external to the thruster body mounted cathodes has shown narrower ion beam divergences for internal cathodes. Work by Raitses et al. [4] on cylindrical Hall thrusters showed that overrunning the cathode, that is, drawing more current through the keeper than necessary, resulted in reduced cathode coupling voltages, reduced near-field plume potentials, and reduced beam divergence.

As discussed in Part I [1], the separatrix has been identified as an important feature in the magnetic field existing in the region between the cathode and the anode. The separatrix is a surface outside of

which all of the magnetic field lines emanating from the outer pole bend back and reconnect with the thruster at the back of the pole. Inside the separatrix, all of the field lines connect directly to the inner pole. Most HET magnetic circuits include this feature.

We have undertaken a series of experiments studying the performance, ion beam properties, and near-field plume properties of a Hall thruster as a function of radial cathode position, cathode mass flow rate, and magnetic field configuration. An extended outer pole (EOP) modifies the magnetic field, moving the position of the separatrix as compared with the original outer pole (OOP), allowing for the effect of the separatrix to be studied (see Part I for details [1]). The thruster performance, specifically, thrust, discharge current, efficiency, and cathode coupling voltage, are discussed in greater detail in Part I. This paper focuses on the ion beam and near-field plume properties and relates them to the results presented in Part I.

II. Experiment

A. Overview

In Part I [1], the design of the experiment, including the modifications made to the thruster to reposition the separatrix, is discussed. A brief recap is presented here. The HET was mounted on a thrust stand, and the cathode was mounted on a linear motion stage such that its orifice could be moved from 40 to 250 mm radially away from the thruster axis while maintaining a fixed axial distance of 30 mm from the thruster exit plane (see Fig. 1). The cathode was mounted with its axis at a 90 deg angle to the thruster axis. A Faraday probe and a retarding potential analyzer (RPA) were placed on a boom mounted on a rotational stage directly above the intersection of the thruster axis and the exit plane. The Faraday and RPA probes were mounted at a distance of 250 mm. A double Langmuir probe was mounted on a two-axis motion table and used to measure the near-field plume plasma properties. A second probe was colocated with the first and served as a backup.

B. Procedure

A detailed description of the experiment is presented in Part I [1]. Therefore, the procedure presented here will focus only on the acquisition of electrostatic probe data. After acquiring thrust data at each cathode location, the ion beam properties were measured. For each cathode mass flow rate and outer pole configuration, RPA and Faraday probe sweeps were performed with the cathode the following radial locations: 40, 50, 60, 70, 80, 90, 100, 120, and 200 mm. In all cases the cathode was positioned axially at $z = 30$ mm. The order in which the cathode positions were investigated was randomized to avoid correlation of positional data with any temporal phenomena. Both probes were mounted at a constant radial distance of 250 mm from the center of the thruster exit plane. The Faraday probe was swept from -90 to $+60$ deg in 2.3 deg increments. The RPA was swept in 10 deg increments over the same range, and $+60$ deg was the maximum angle at which these probes could be placed without running into the cathode or cathode mount.

After acquiring all of the RPA and Faraday probe data, near-field plume plasma properties were measured with a double probe with the cathode positioned axially at $z = 30$ mm and radially at $r = 50$, 60, 80, 100, 120, and 200 mm. Again, the positions were chosen in random order. The plasma properties were measured in a rectangular area extending from $r = -180$ to $r = 180$ mm and from $z = 5$ to $z = 105$ mm. The sampling grid spacing varied between 5 mm very near the thruster, to 20 mm in the radial extremes. The double probe was moved through the grid points first in the radial direction, and then in the axial direction in a pattern chosen to minimize probe heating. Further details can be found in Sommerville's dissertation [5].

C. Equipment

The Hall-effect thruster used in this experiment was an Aerojet BPT-2000. Details about the thruster, including the modifications for the extended outer pole experiments, are discussed in Part I [1]. Part I also discusses the cathode, vacuum facility, mass flow controllers, and thrust stand. The remainder of this section will focus on the electrostatic probes used in these experiments. Greater detail on the probe construction is available in Sommerville's dissertation [5].

1. *Faraday Probe*

The Faraday probe used was a guard-ring-type planar probe. The probe electrode was a tungsten rod 2.4 mm in diameter. The guard was separated from the probe by an alumina tube with an outer diameter of 4.75 mm. The guard ring, made of stainless steel, surrounds the alumina. The outer diameter of the guard ring was 10 mm. Except for the face, the guard ring was spray coated with boron-nitride to reduce amount of current collected by the ring.

The current to the probe electrode was passed through a shunt resistor, and the voltage across the resistor was amplified by an op-amp circuit, and then measured with a computer-based data acquisition system. The voltage to the guard ring was controlled via a field-effect transistor (FET) operating as a voltage-controlled resistor [5]. This circuit ensured that the guard ring was biased to the same potential as the probe. Both electrodes are biased at -15 V below

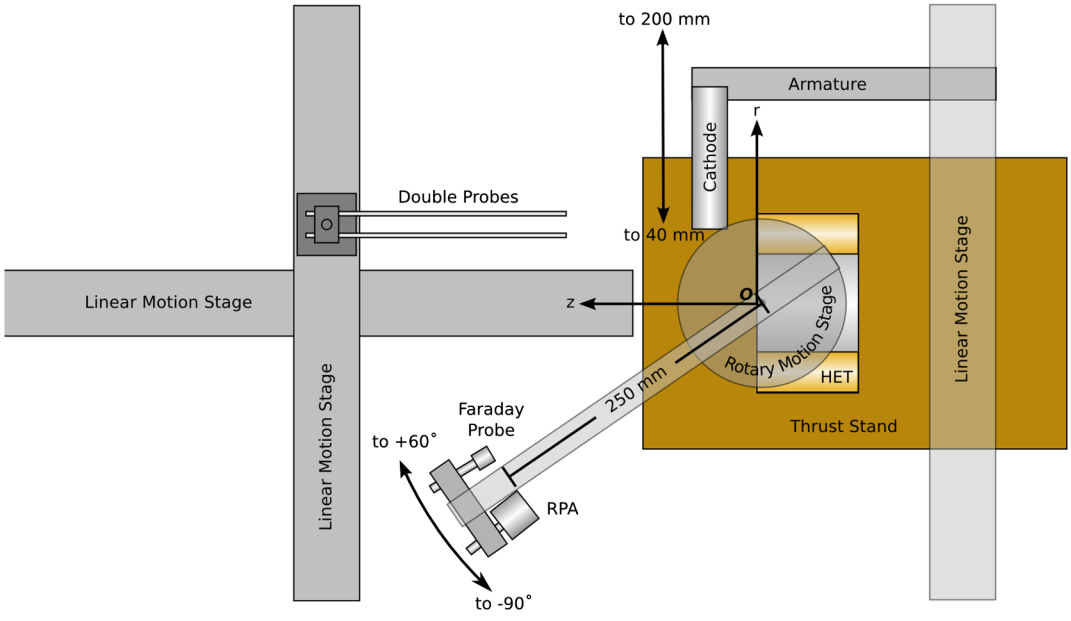

Fig. 1 Experimental setup (in color online).

ground to repel plasma electrons. This value was chosen after sampling the probe current at higher voltages and finding no change for voltages below −15 V.

The probe was swept from an angle of −90 to +60 deg. At each angular position, the voltage from the shunt resistor amplifier was measured by a computerized data acquisition system, and converted into a current. At each location, 1000 current samples were read at a rate of 10 kHz and averaged. Current density was then calculated from the probe current according to

$$j = \frac{4I_{\text{probe}}}{\pi D_{\text{probe}}^2} \tag{1}$$

2. Retarding Potential Analyzer

The RPA used in the experiments is a four-grid design. The first grid is a floating grid, designed to isolate the plasma from the various potentials applied to the remaining grids. The second grid is an electron repeller, which is biased negative relative to plasma potential to prevent electrons from entering the remainder of the probe. The third grid is the ion repeller. This grid is swept across the desired voltage range and allows only those ions with energies above the grid potential to pass through to the collector. The final grid is a secondary electron suppression grid. This is designed to force any secondary electrons ejected from the collector by the impact of an ion to return to the collector.

The grids on the RPA are made from stainless-steel mesh with 0.139-mm spacing and a 30% open-area fraction. Each grid is spaced 2.54 mm apart from the next. The orifice of the probe is a circle 12.7 mm in diameter. This diameter is maintained through the length of the probe, to the equally sized collector, which is simply a grounded, stainless-steel plate.

Current to the collector is sensed by a current amplifier/current-to-voltage converter manufactured by Femto. The output voltage is measured with a computerized data acquisition system. The sweeper grid is swept from 0 to 300 V in either 1 or 0.5 V steps using a Keithley 2410 source-meter. The sweeps were run at the source-meter's fastest acquisition rate, which is approximately 860 Hz. As configured, the source-meter had a source accuracy of ±300 mV, and a measurement accuracy of 1%. Five sweeps were taken and averaged to mitigate measurement noise. The electron repeller and secondary suppression grids are biased with a dc power supply to −15 V. Test traces were also taken at −30 V on centerline, where the plasma potential was expected to be highest. No differences were discernible. From this we concluded that −15 V sufficiently repelled electrons.

To reduce the RPA trace, a cubic spline was fit to all of the data acquired. This process was done semi-automatically. A computer program guessed the best spline to fit the data. However, manual interaction was required to choose an appropriate number of spline knots, and to slightly modify the spline to achieve the best visual fit of the spline to the raw data. The spline was then normalized so that its maximum current value (at $V = 0$ V) was set to 1 and at the maximum sweep voltage of 300 V the current value was 0. The negative of the derivative of the normalized spline is the ion voltage distribution function (IVDF):

$$f(V) = -\frac{\mathrm{d}I_{\text{spline}}(V)}{\mathrm{d}V} \tag{2}$$

If all ions are assumed to be singly-ionized, this is equivalent to the ion energy distribution function (IEDF). The voltages used in this equation are not corrected for plasma potential. By doing so, we determine the energy that the ion would have had had it not been captured by the probe but continued unimpeded to the tank wall.

3. Double Probe

The double probe configuration [6] lessens or eliminates three problems associated with single Langmuir probes. First, because the probe is limited to drawing ion saturation current, it is less disturbing to the plasma [6]. Second, because the motion of the ions, rather than the electrons govern the collection of current, the probe is much less sensitive to errors due to the presence of magnetic fields [7]. Finally, it is less likely that sheath effects will disturb the probe trace to the point that the "knees" of the trace disappear, making analysis difficult or impossible.

If V is the voltage applied between the two probes and the ion saturation current is given by

$$I_{i,\text{sat}} = en_eA\sqrt{\frac{kT_e}{m_i}} \tag{3}$$

then an ideal double probe trace takes the shape of a hyperbolic tangent given by [6]:

$$I(V) = I_{i,\text{sat}} \tanh\left(\frac{1}{2}\frac{eV}{kT_e}\right) \tag{4}$$

A typical (nonideal) double probe trace is shown in Fig. 2.

Analyses of double probe data using the only the simple expression in Eq. (4) are subject to errors that may arise due to sheath expansion. To overcome these problem, Peterson and Talbot [8] derived a theoretical approach to single and double Langmuir probe traces which accounts for sheath expansion and has been shown to be robust [9]. The method involves adjusting the plasma parameters to minimize the difference between the acquired data and the theoretical curve.

Defining the nondimensional potential as

$$\chi = \frac{eV}{kT_e} \tag{5}$$

we can then define the nondimensional potentials of each probe, χ_1 and χ_2, as well as the nondimensional floating potential, χ_f, each with respect to the plasma potential. Note that these values will always be negative as the double probe electrodes never reach plasma potential. The nondimensional potential difference between the probes and the floating potential are defined as

$$\psi_1 = \chi_f - \chi_1 \tag{6}$$

$$\psi_2 = \chi_2 - \chi_f \tag{7}$$

Adding Eq. (7) to Eq. (6) yields the nondimensional voltage applied between the probes

$$\psi = \psi_2 + \psi_1 = \chi_2 - \chi_1 \tag{8}$$

The current collected at each probe is given by an empirical fit to Laframboise's [10] theoretical treatment of Langmuir probe dynamics:

$$I_1 = I_{\text{sat},1}(\beta - \chi_f + \psi_1)^\alpha \tag{9}$$

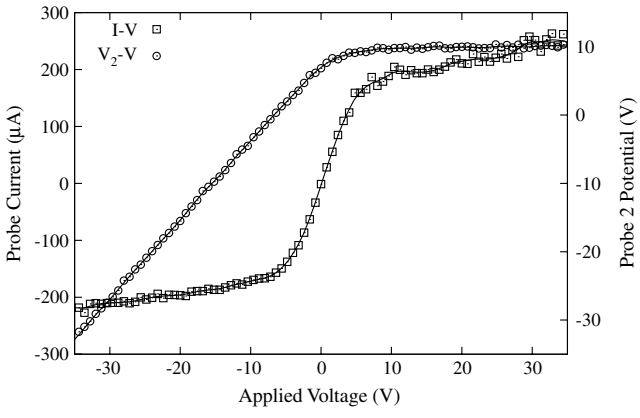

Fig. 2 Typical double-Langmuir probe trace.

$$I_2 = I_{\text{sat},2}(\beta - \chi_f - \psi_2)^{\alpha} \tag{10}$$

where α and β are given by

$$\alpha = 2.900/[\ell_n(r_p/\lambda_d) + 2.300] + 0.070(T_i/T_e)^{0.750} - 0.340 \tag{11}$$

$$\beta = 0.070 + \{5.100 + 0.135[\ell_n(r_p/\lambda_d)]^3\} \tag{12}$$

for probes attracting ions. Recall that neither probe reaches plasma potential, so neither probe attracts electrons. With the ion currents to each probe, the total current through the circuit is given by

$$I(\psi) = \frac{I_1(A_2/A_1)\exp(\psi/2) - I_2\exp(-\psi/2)}{\exp(\psi/2) + (A_2/A_1)\exp(-\psi/2)} \tag{13}$$

Equation (13) represents a theoretical expression for the *I-V* trace of a double probe given the following parameters: T_e, T_i, n_e, r_p, and χ_f. Of these, r_p is known, and T_e and n_e will be adjustable fit parameters. The nondimensional floating potential can be determined theoretically given T_e, T_i, and n_e from the implicit equation

$$\chi_f = \frac{1}{2}\ell_n\left(\frac{m_e}{m_i}\right) + \alpha\,\ell_n(\beta - \chi_f) \tag{14}$$

That leaves T_i. Fortunately, in HET plume plasmas, as in many other plasmas, the ion temperature is much lower than the electron temperature, typically near 500°C [11]. Furthermore, only in α [Eq. (11)] is affected by T_i, and if $T_i \gg T_e$ then it is a weak effect. Therefore, an estimate is sufficient. In this work, a value of 500°C is used for all analyses.

As was noted above, the floating potential with respect to ground can be easily determined from the plot of the potential of one of the probes with respect to ground versus the applied voltage. Using the knowledge of the floating potential and Eq. (14) the plasma potential with respect to ground can be determined from the Peterson and Talbot [8] fit to the *I-V* trace of a double probe.

However, if the entire trace of probe potential versus applied voltage is available, as in the V_2-V curve of Fig. 2, this can also be used to refine the analysis of the double probe trace. Again, according to Peterson and Talbot [8], the potential of probe 1, that is, the probe which swings negative when a positive voltage is applied, is given implicitly by

$$\psi_1(\psi) = -\ell_n\left[\left(1 + \frac{\psi_1}{\beta - \chi_f}\right)^{\alpha} + \frac{A_2}{A_1}\left(1 + \frac{\psi_1}{\beta - \chi_f} - \frac{\psi}{\beta - \chi_f}\right)^{\alpha}\right] + \ell_n\left[1 + \frac{A_2}{A_1}\exp(\psi)\right] \tag{15}$$

From Eq. (8), the voltage of probe 2 is simply

$$\psi_2(\psi) = \psi - \psi_1(\psi) \tag{16}$$

With these equations, it is possible to analyze not only the *I-V* trace of the double probe, but also either V_{probe}-V_{applied} trace and thereby increase confidence in the analysis. Using the theory present here, we devised a numerical fitting algorithm to determine the plasma parameters based on the double probe traces acquired [5].

The double probes used in these experiments consisted of a double bore alumina tube approximately 300 mm in length with an outside diameter of 4.76 mm (3/16 in.) and a bore diameter of 1.6 mm (0.063 in.). The alumina used was at least 99.5% Al_2O_3 with the remainder being trace elements [12]. Tungsten wire of 0.5 mm (0.02 in) diameter was fed through each bore. The end of the tube was sealed with a ceramic adhesive leaving 4 mm of each electrode exposed. Each electrode was approximately 4 mm from the other, ensuring that the probes were several debye lengths apart. The diameter of the wire was chosen as a good compromise between maximizing r_p/λ_d in all regions of the plume and minimizing probe size.

At each grid point, the applied voltage was swept between −40 and 40 V in 1 V increments. The sweep voltage was applied and the current measured by a Keithley 2410 source-meter. The source-meter also triggered a data acquisition system which, through an isolated analog input module, simultaneously measured the potential of one of the two double probe electrodes (Probe 2) with respect to ground. Plasma parameters were extracted from the traces by the Peterson and Talbot [8] method discussed above.

Probe heating was an issue when the probe was positioned in the hot, dense ($T_e \sim 10$ eV, $n_e \sim 5 \times 10^{17}$ m^{-3}) plasma very close to the thruster exit. A study of the probe heating showed that it resulted in an increase in the electron temperature measured by the probe, which, in turn, affects the calculated plasma potential. The effect was temporary: if the probe was removed from the hot plasma, allowed to cool and then reintroduced it, would yield the same results as it did at first. Therefore, probe ablation was not the source of the error. Furthermore, because the probe was not visibly emissive, it is also unlikely that electron self-emission was the problem. A more detailed discussion is available in Sommerville's dissertation [5]. To mitigate the effects of probe heating, a scan pattern was chosen such that the probe spent minimal time in the hot plasma by moving first in the radial direction, and then in the axial direction.

III. Efficiency Components

A. Method

With ion current densities and energy distributions it is possible to break down the efficiency into its constituent loss mechanisms with the goal of identifying the significant causes of change in efficiency. Following, Larson et al. [13] and Ross and King [14], we decompose efficiency into the loss mechanisms shown in Table 1. The following series of Eqs. (17–23) show how each of these efficiencies are broken out of the total efficiency

$$\eta = \frac{T^2}{2\dot{m}P} \tag{17}$$

$$= \frac{\frac{1}{2}\dot{m}\langle \mathbf{v}\rangle^2}{I_d V_d} \tag{18}$$

$$= \frac{\langle \mathbf{v}\rangle^2}{\langle \mathbf{v}^2\rangle}\frac{\frac{1}{2}\dot{m}\langle \mathbf{v}^2\rangle}{I_d V_d} \tag{19}$$

$$= \underbrace{\frac{\langle v\rangle^2}{\langle v^2\rangle}}_{\eta_{vdf}}\underbrace{\langle\cos(\theta)\rangle^2}_{\eta_\theta}\frac{\frac{1}{2}\dot{m}\langle \mathbf{v}^2\rangle}{I_d V_d} \tag{20}$$

$$= \eta_{vdf}\eta_\theta\underbrace{\frac{e\dot{m}/m}{I_d}}_{\eta_I}\frac{\frac{1}{2}m\langle \mathbf{v}\rangle^2}{eV_d} \tag{21}$$

$$= \eta_{vdf}\eta_\theta\underbrace{\frac{I_b}{I_d}}_{\eta_I}\underbrace{\frac{\frac{1}{2}m\langle \mathbf{v}^2\rangle}{e(V_d + V_{cg})}}_{\eta_V}\underbrace{\frac{V_d + V_{cg}}{V_d}}_{\eta_{Vcg}} \tag{22}$$

$$= \eta_{vdf}\eta_\theta\eta_I\eta_V\eta_{Vcg} \tag{23}$$

No attempt is made to correct for ionization fraction in these equations, or the proceeding analysis. That is to say, we assume that all ions are singly charged. Because of this, the values calculated for η_{vdf} are most likely slightly too large, while those calculated for η_V are too small. The magnitude of this effect will be addressed in Sec. III.B.

The various expectation values are calculated by a weighted average according to the following equation:

Table 1 Efficiency loss mechanisms

Efficiency	Sym.	Definition	Description	How to measure
Beam divergence	η_θ	$\langle\cos(\theta)\rangle^2$	Ion velocity components not parallel to the thruster axis tend to cancel and do not generate thrust	Integrate the Faraday-probe-derived current densities to find the expectation value of $\cos(\theta)$
Voltage utilization	η_V	$\frac{\frac{1}{2}m\langle\mathbf{v}^2\rangle}{e(V_d+V_{cg})}$	Not all ionization takes place at the top of the potential hill. Because of this, ions do not receive the full amount of energy available.	Integrate IEDF and current density data, similar to the process for η_{vdf}, and divide by the sum of the measured V_d and V_{cg}
Velocity distribution	η_{vdf}	$\frac{\langle v\rangle^2}{\langle v^2\rangle}$	Inefficiency due to the spread in 1-D velocity space of the ions	Calculate this efficiency at each angle from the IEDF. Perform a weighted average of all angles, weighting by current density and solid-angle.
Current utilization	η_I	I_b/I_d	The "recycle" current "leaks" from the cathode to the anode without directly creating thrust in the form of beam ions.	Integrate Faraday-probe-derived current densities to obtain I_b and divide by discharge current (I_d) measured by power supply
Cathode coupling	η_{Vcg}	$\frac{V_d+V_{cg}}{V_d}$	The voltage at the cathode floats below ground is not available to accelerate ions. Note that V_{cg} is always negative.	Measure the cathode coupling voltage

$$\langle x\rangle = \frac{\int_{-90^\circ}^{60^\circ}\int_0^{300\ \mathrm{V}} x(V,\theta)f(V,\theta)j(\theta)R^2\sin(|\theta|)\,\mathrm{d}V\,\mathrm{d}\theta}{\int_{-90^\circ}^{60^\circ}\int_0^{300\ \mathrm{V}} f(V,\theta)j(\theta)R^2\sin(|\theta|)\,\mathrm{d}V\,\mathrm{d}\theta} \tag{24}$$

Note that this equation assumes azimuthal symmetry for each half of the thruster (the cathode side where r and $\theta > 0$, and the opposite side where r and $\theta < 0$). Since the data to be integrated are discrete, the inner integral is first performed at each available angle using Simpson's rule. The results of these integrations are then linearly interpolated, multiplied by the current densities, and integrated across θ. Where RPA data are unavailable, the θ integration range is truncated.

Strictly speaking, the separation of η_{vdf} and η_θ in Eq. (20) is only valid if the IEDF is independent of angle. However, the conceptual separation of the two loss mechanisms is convenient for understanding the source of inefficiency. In the acquired data, the IEDFs are consistant across the angular range where the majority of the current is detected, typically between −40 and 40 deg in this work, which minimizes the impact of this invalid math. Typically, we find $|\eta_\theta\eta_{vdf} - \langle\mathbf{v}^2\rangle/\langle\mathbf{v}^2\rangle| \sim 0.05$.

B. Results

The results of this efficiency decomposition are shown in Fig. 3, along with the measured efficiency and the calculated total efficiency. The total efficiency is the product of all efficiency components according to Eq. (23) and is denoted by η_{prod}. Total efficiencies are plotted with solid lines, while efficiency components are plotted with dashes. The efficiency η_a is the total efficiency as measured by the thrust stand and power supply telemetry, as discussed in Part I [1].

Due primarily to facility effects, the absolute uncertainty on the integrated beam currents used to calculate the current utilization efficiency are estimated at $+0\%/-40\%$. This estimate is based on work done by Rovey et al. [15] with magnetically filtered Faraday probes. In other words, the measurement should be thought of as an upper limit of the actual value. This uncertainty propagates directly through to the uncertainty in η_I. The beam divergence is calculated from the same data, but the uncertainty in magnitude of the current density affects the calculation of beam divergence less strongly. Using an unfiltered probe, Rovey et al. found 90% beam divergence angles[‡] that were reduced from 30 deg probe to between 25 and 28 deg when using a probe that filtered out charge-exchange ions. Based on this, we estimate the uncertainty in beam divergence (defined in this work as $\langle\theta\rangle$) at 5 deg. Typical beam divergences in this work are around 35 deg. Here again, the uncertainty is primarily in the negative direction. That is, actual divergence is probably less than 35 deg. Propagating the uncertainty through the equation for η_θ yields an uncertainty of $+8\%/-0\%$.

[‡]The 90% beam divergence angle is the angle to which, when integrating beam current from 0 degrees, will include 90% of the total beam current.

Because of the manual spline step in the processing of the RPA data, a further manual step was required to estimate the uncertainties in those efficiencies based on the IEDF, that is, η_V and η_{vdf}. At one operating condition, the RPA traces at every angle were splined not only with the best fit spline, but with four additional splines: the highest voltage (spline most right-shifted), lowest voltage (spline most left-shifted), steepest sloped, and shallowest sloped splines that could be reasonably be drawn through the data. The first two allow an estimate on the uncertainty in η_V, while the second two allow for an estimate on the uncertainty in η_{vdf}. This procedure was done for all of the IEDFs at one of the noisier operating conditions (OOP, $\dot{m}_c = 5$ SCCM, $r = 70$ mm). From this, we estimated the uncertainty on η_V at ±20% and the uncertainty on η_{vdf} at ±4%.

In addition to the to these uncertainties resulting from random error, we must also consider the systematic error that arises because we did not take into account ionization fraction. To estimate this, make the assumption that the IVDFs of all species are identical. Then, using the ionization fractions an estimate of the ionization fraction, we can generate estimated IEDFs based on the measured IVDFs according to

$$f_{\mathrm{IEDF}}(E) = \sum_{i=1}^{N} q_i F_i f_{\mathrm{IVDF}}(E/q_i) \tag{25}$$

Using the measured IVDFs and the ionization fractions reported by Linnell for a HET running krypton as a best guess, we estimate an additional +10 percentage point error for η_V and an additional −2 percentage point error for η_{vdf}.

Proper handling of asymmetric, systematic uncertainties requires knowledge of the the probability distribution functions for the measurements. Unfortunately, for the Faraday-probe-derived data, no such function is available. Therefore, to propagate the errors through to η_{prod} the following procedure is used. The percentage uncertainties resulting from the random errors associated with the η_V and η_{vdf} are added in quadrature. The random error on η_{Vcg} is negligible compared with these quantities and is disregarded. Then, the systematic errors associated with η_I, η_θ, η_V, and η_{vdf} are added linearly [16]. For the random uncertainties of an efficiency component η_x denoted by $U_r(x)$, and the positive or negative systematic uncertainties of η_x denoted by $U_\pm(x)$, this is expressed mathematically as:

$$\frac{U_\pm(\mathrm{prod})}{\eta_{\mathrm{prod}}} = \pm\left[\sum_x\left(\frac{U_r(x)}{\eta_x}\right)^2\right]^{1/2} + \sum_x \frac{U_\pm(x)}{\eta_x} \tag{26}$$

The results of the propagation are displayed in the error bars of η_{prod} in Fig. 3.

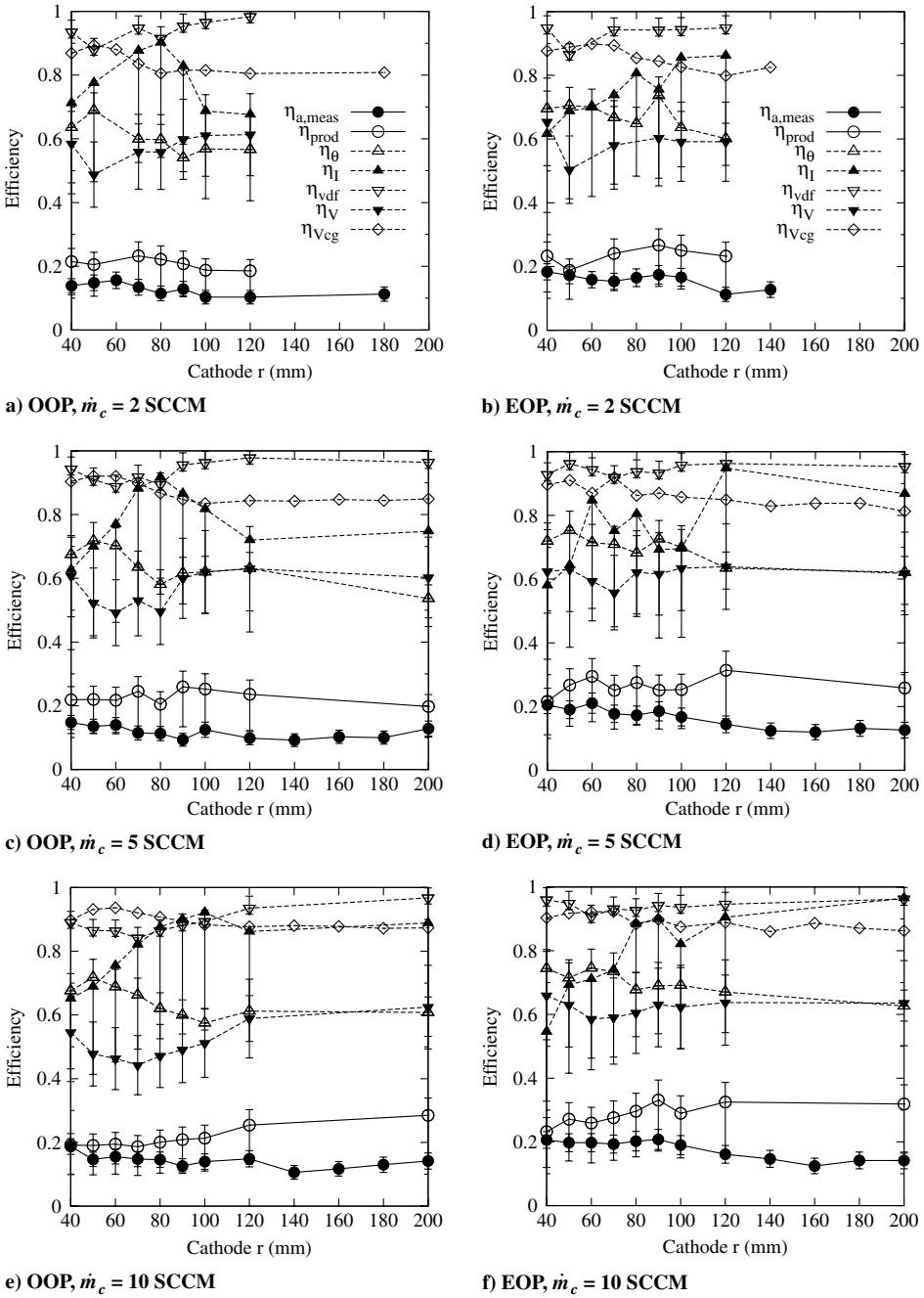

a) OOP, $\dot{m}_c$ = 2 SCCM **b) EOP, $\dot{m}_c$ = 2 SCCM**

c) OOP, $\dot{m}_c$ = 5 SCCM **d) EOP, $\dot{m}_c$ = 5 SCCM**

e) OOP, $\dot{m}_c$ = 10 SCCM **f) EOP, $\dot{m}_c$ = 10 SCCM**

Fig. 3 Efficiency component breakdown.

C. Discussion

Inefficiency in voltage utilization and beam divergence are the most significant contributions to the inefficiency of the thruster, across all cases. The voltage utilization is seen to decrease slowly as the cathode is brought in from 200 mm, decrease more rapidly starting at 120 mm to a minimum located near 60 mm and then increase as the cathode is brought to 40 mm. The trends in velocity distribution efficiency follow closely that of η_V. These trends could be explained by increased cathode propellant ingestion as the cathode is brought closer. Ingested cathode neutrals are likely to be ionized lower in the potential hill, before they drift back into the higher potential regions inside the discharge chamber. The lower energies of the cathode ions mixed in with the anode ions would result in both a lower η_V and a lower η_{vdf}. Additional evidence for this interpretation can be found in that the depth and breadth of the decrease in these efficiency components between 40 mm and 100 mm increases with increasing $\dot{m}_c$, at least for the OOP data. If this interpretation is correct, it should be noted that the decrease in this efficiency component is a little misleading. The addition of the impulse of the low velocity ions to the thrust of the system is still an increase in thrust, and is better than simply having the cathode neutrals expelled into space.

Furthermore, the decrease in η_V should be offset by an increase in η_I, as both I_b increases by, at most, the same amount as I_d.[§] Indeed, this is seen in some of the cases, particularly of the OOP data, but not in all. The current utilization efficiency for the OOP exhibits a bump between 40 and 120 mm, with the maximum occurring between 80 and 100 mm. The trends are less clear for the EOP data. The bump may be explained in part by an increase in cathode propellant ingestion. However, it is too large for this to be the only effect, particularly in the 2 standard cubic centimeter per minute OOP case. As discussed in terms of discharge current in Part I [1], the maximum

[§]This assumes that every cathode neutral ingested and ionized is captured by the Faraday probe. If that is true, then η_I must increase since, $\frac{I_b+I_{\text{ingested}}}{I_d+I_{\text{ingested}}} > \frac{I_b}{I_d}$, for $I_b < I_d$.

increase in current (both I_b and I_d) possible is 0.14 A. At greater radial cathode positions the discharge currents are approximately 3 A and η_I is approximately 0.7. If all of the cathode propellant was ingested and ionized, this would result in an improvement in efficiency from 0.7 to 0.71, according to:

$$\eta_{I,\text{improved}} = \frac{I_{b,\text{improved}}}{I_{d,\text{improved}}} = \frac{\eta_I I_d + I_{\text{ingested}}}{I_d + I_{\text{ingested}}} \tag{27}$$

Even in the 10 SCCM case only about a 5% improvement is possible. Clearly another process is at work on η_I, η_V, and η_{vdf}.

The beam divergence efficiency has nearly an opposite trend to that of η_V. It is relatively flat beyond 120 mm and exhibiting a bump between 40 and 120 mm. One also notes that η_{Vcg} varies almost in lock-step with η_θ. This will be further explored in Sec. IV.

All efficiency components except η_I are consistently higher for the EOP than for the OOP. This is not surprising, given the improved behavior or the EOP, as discussed in Part I [1]. Furthermore, the trends that are similar between the EOP and the OOP seem shallower and broader for the EOP. This suggests that the position of the separatrix may be playing a roll in the efficiency. It is also possible, however, that it is merely an effect of the differing magnetic fields used in the two experiments.

IV. Plume Properties

A. Results

Figures 4 and 5 show sample results from the measurement of the plume properties. These figures plot T_e, n_e, and V_f. Using these measurements and Eq. (14), V_p was calculated and the results were also plotted. A sketch of the thruster and the cathode show the position of the plume data with respect to these objects. The modeled magnetic field lines are overlaid in black lines. The white dots show the location of each individual measurement. A cost score, the parameter used in the fitting routine [5], was used to automatically reject any trace which did not sufficiently match the probe theory. The maximum allowable cost was chosen after manually inspecting several traces and their theoretical fits. Data points removed by this process have their corresponding dot removed from the figure. Note that this rejection only applies to the values for T_e, n_e, and V_p. The value of V_f is a single-point measurement and, therefore, independent of the quality of the match between the measured probe trace and theory. The plasma property contours were created by interpolating the accepted data points onto a 1 mm rectangular mesh using a natural neighbor interpolation [17].

It is likely that the largest contribution to the error in these probe measurements comes from errors due to probe heating. A measure of the uncertainty can be made by examining the change in the measured parameters for a probe in a stationary position in a hot, dense region of the plume. The longest that the probe in the actual sweep pattern was exposed to dense, hot plasma was approximately 1 min. Double probe traces were taken with the probe at $r = 0$ mm, $z = 10$ mm at one sweep per second for 60 s. The standard deviations of the resulting analyses of T_e and n_e were 6 and 15%, respectively. The standard deviation in V_f was a negligible 1%. The standard deviation in V_p was 5%. An additional systematic source of error in the measurement of n_e is in the measurement of the area of the probes. The diameter of the probe is well established as it is manufactured to a tolerance of 2%. However, the exposed length of the probe was measured by hand using calipers and was not more accurate than 0.5 mm on length measuring 4 mm. This adds an additional error of about 12.7% arising from the uncertainty in probe area to the estimate of the uncertainty on the density. Adding the uncertainties in quadrature, the uncertainty estimate on n_e is 20%.

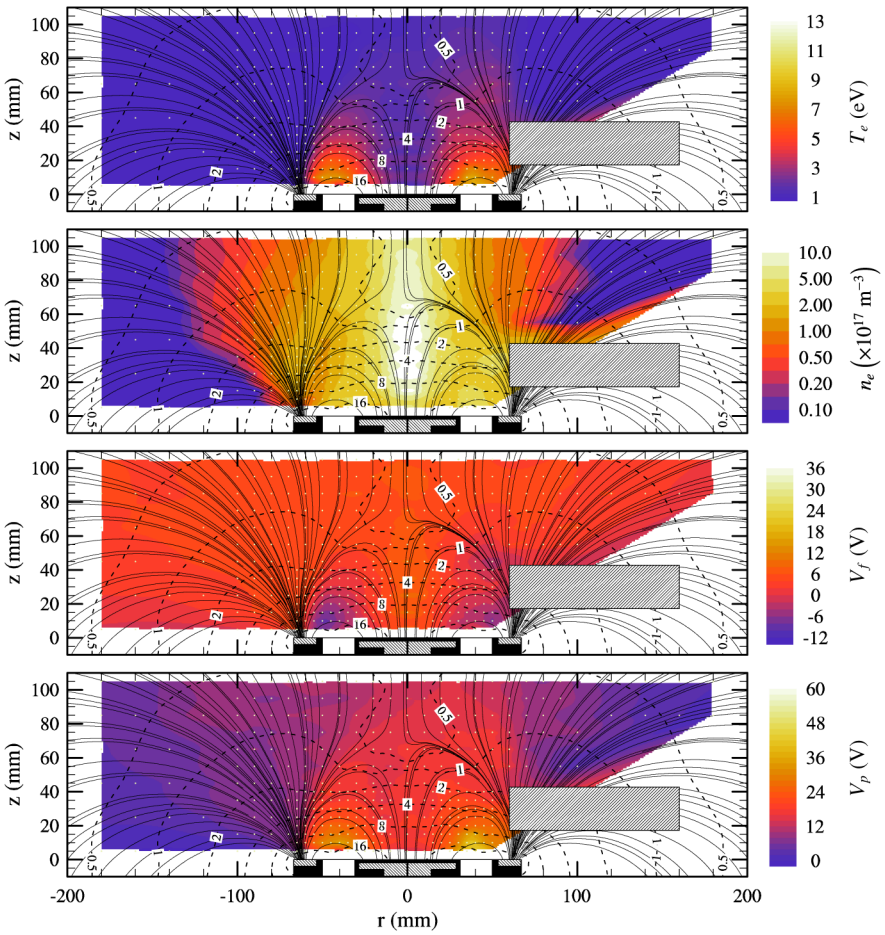

Fig. 4 Plasma properties on the thruster with the OOP with $\dot{m}_c = 10$ SCCM and the cathode at $r = 60$ mm (in color online).

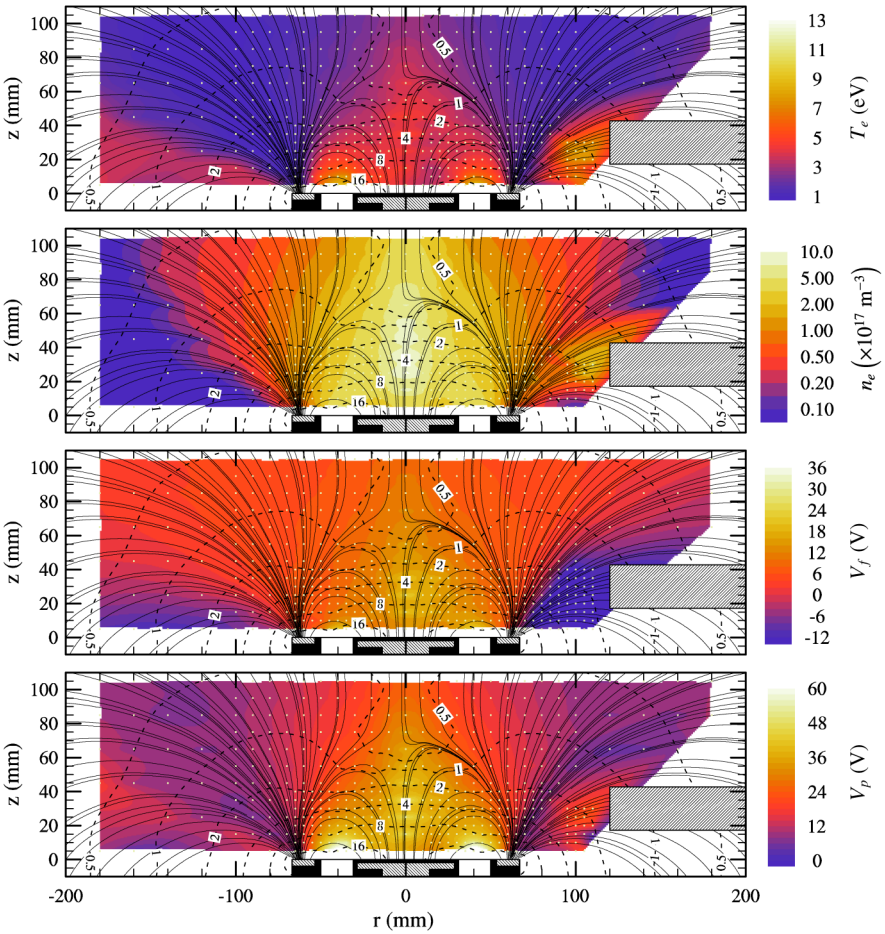

Fig. 5 Plasma properties on the thruster with the OOP with $\dot{m}_c = 10$ SCCM and the cathode at $r = 120$ mm (in color online).

B. Discussion

Several features of the plume properties common to most of the operating conditions can be seen in Figs. 4 and 5. First, one sees that T_e, V_f, and V_p are lower everywhere, and particularly in the near field, when the cathode is placed at 60 mm as compared with when it is at 120 mm. Meanwhile the electron density remains relatively constant, perhaps becoming slightly more divergent and less dense in the 120 mm case. Figure 6 shows the monotonic increase in plasma potential for every cathode position measured with the thruster operating with the EOP and $\dot{m}_c = 10$ SCCM. Inspection of the data for the rest of the operating conditions showed similar trends. In Fig. 6, one notes the particular increase in near-field potential between when the cathode is positioned essentially on the separatrix at 80 mm and when it is outside the separatrix at 100 mm. This will be further explored in Sec. IV.C.

The radial striations in the plasma potential when the cathode is positioned at 120 and 200 mm are the result of double probe heating. Despite the choice of scan pattern, this effect could not be completely eliminated when the electron temperatures were high given our current equipment. A fast scanning probe would solve this problem. Fortunately, the striations make it easy to see when probe heating was an issue and when it was not.

By comparing any of the plots of Fig. 6 to the plasma potential plots in either Fig. 4 or Fig. 5, one can see the plasma containment effect of the separatrix. The hot, high-potential plasma is trapped within the separatrix. Note that near $z = 10$ mm this higher potential plasma does not cross beyond $|r| = 60$ mm, the location of the separatrix for the OOP. Outside the separatrix, cooler, lower potential plasma prevails.

In addition to the containment, the effect of the azimuthal drift arising from the Hall current may also be visible. In Fig. 5 one notes the high electron temperature and high plasma potential just outside the orifice of the cathode and a corresponding region of low floating potential. On the opposite side of the figure, roughly in the region, -200 mm $< r < -100$ mm and $0 < z < 30$ mm, a similar elevation in T_e and V_p and depression in V_f can be seen. This effect can also be seen in most of the floating potential plots of Fig. 7. In fact, there is also evidence of this reflection of the cathode plasma inside the separatrix when the cathode is positioned in or near the separatrix. This can be seen in the depression in V_f on both positive and negative r positions in Fig. 7 when the cathode is at $r = 50$ mm and $r = 60$ mm. The effect was particularly striking in all cases where the cathode was positioned at $r = 50$ mm. The most reasonable conclusion is that the cathode plasma is "smeared out" around the periphery of the thruster, because of the tendency of electrons to drift in the $\mathbf{E} \times \mathbf{B}$ direction. This smearing, however, is not perfect and can be seen as an asymmetry in plasma parameters for cathode locations greater than 100 mm. When the cathode is positioned in or near the separatrix, this asymmetry is much less noticeable.

One of the most striking features of the plume plasma is the formation of a double layer [18,19] between the cathode and the anode along magnetic field lines. This can be seen in the trapping of the hot, high-potential plasma from the cathode, apparently along magnetic field lines, as seen in Fig. 5. Again, the floating potential shows the effect most clearly, owing to the low uncertainties in the data. Figure 7 shows the floating potential maps for each of the cathode positions when the thruster was operated with $\dot{m}_c =$ 10 SCCM and the OOP. As the cathode is moved in from its farthest point, the sharp boundary between the cathode-region plasma and the anode-region plasma is seen to push closer and closer to the separatrix, always falling along the magnetic field lines. After crossing the separatrix, a depression in potential appears to be confined on the field lines within the separatrix. The same behavior was seen, to one extent or another, in most of the plume data.

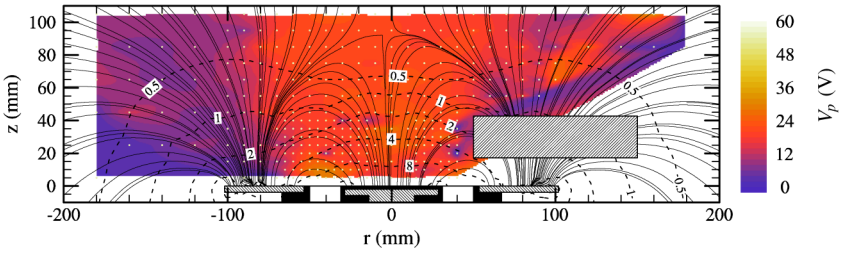

a) Cathode r = 50 mm

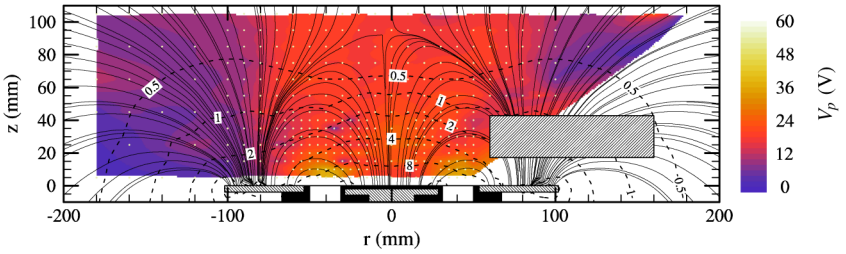

b) Cathode r = 60 mm

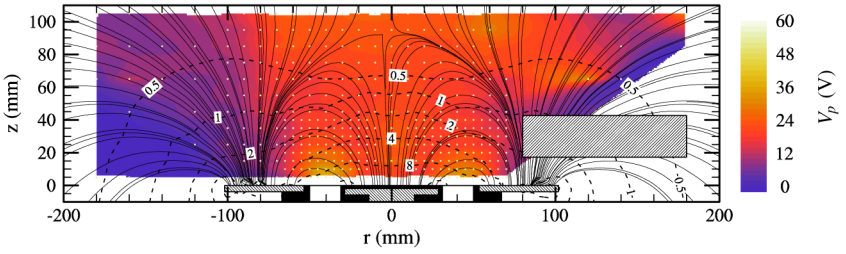

c) Cathode r = 80 mm

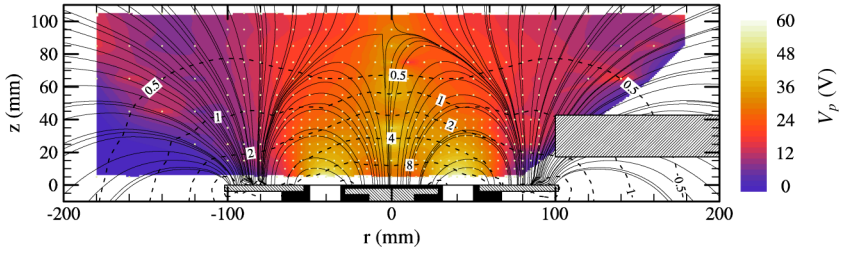

d) Cathode r = 100 mm

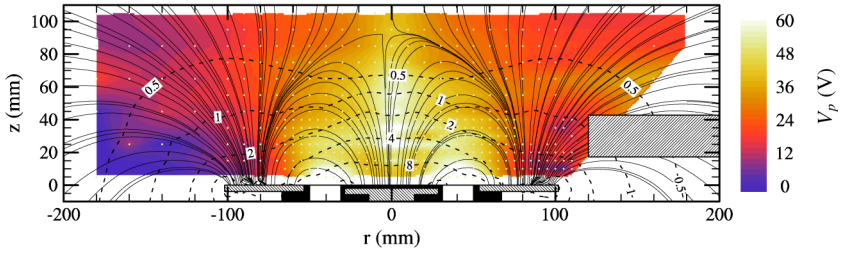

e) Cathode r = 120 mm

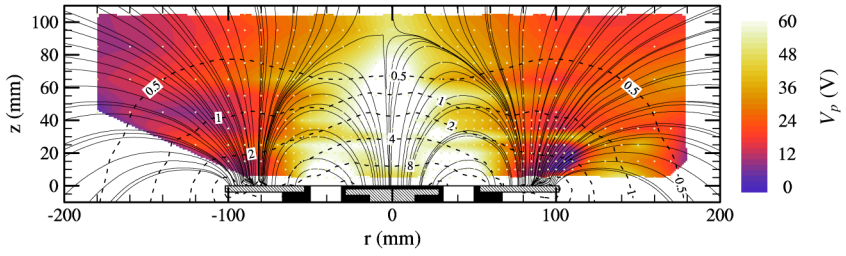

f) Cathode r = 200 mm

Fig. 6 Plasma potential plots for the thruster operating with the EOP and $\dot{m}_c$ = 10 SCCM. The near-field plasma potential increases with cathode position (in color online).

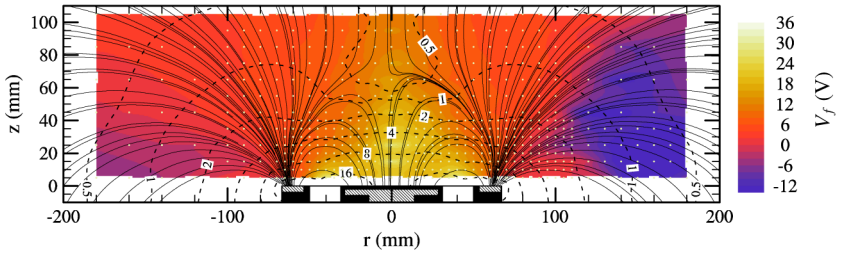

a) Cathode r = 200 mm

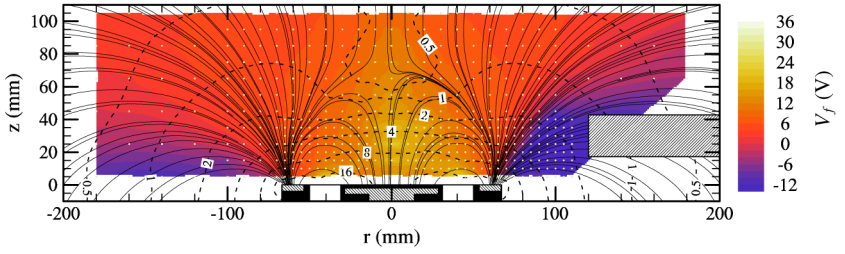

b) Cathode r = 120 mm

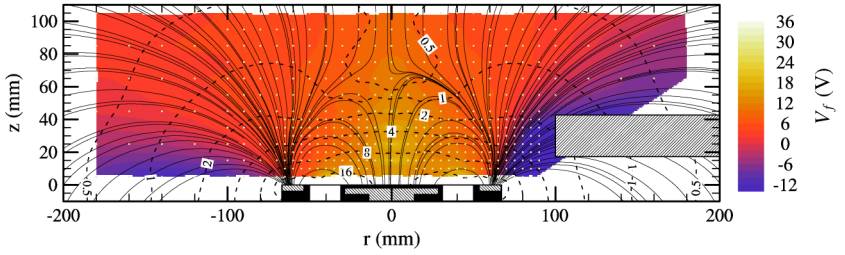

c) Cathode r = 100 mm

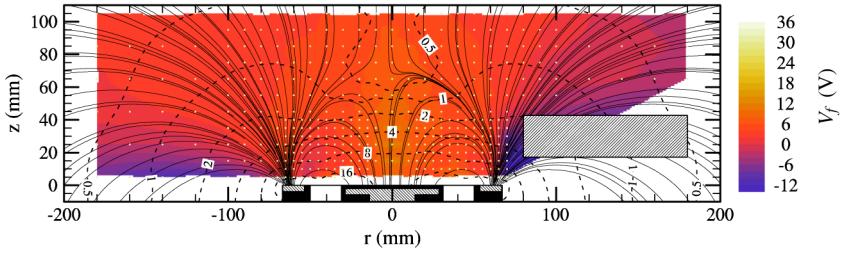

d) Cathode r = 80 mm

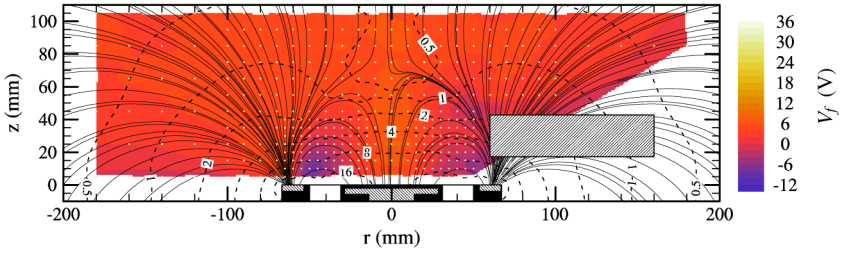

e) Cathode r = 60 mm

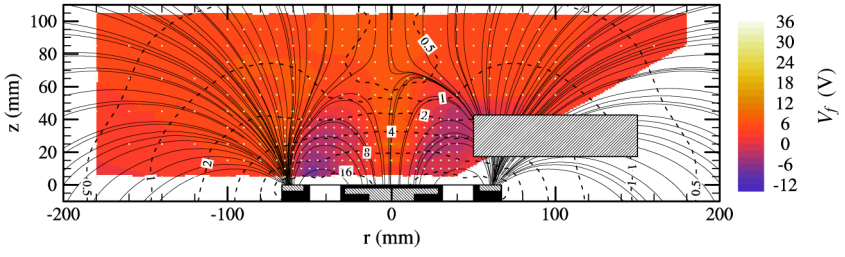

f) Cathode r = 50 mm

Fig. 7 Floating potential maps exhibit a double layer between the cathode and beam plasmas (in color online).

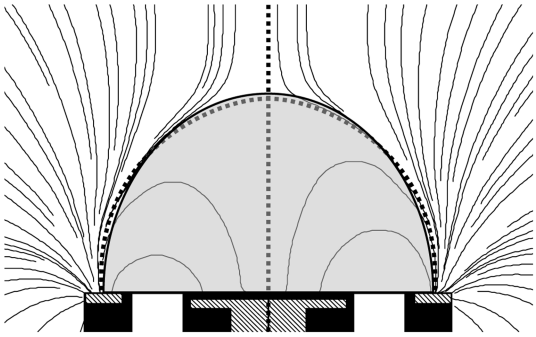

Fig. 8 Area of plume property averaging overlaid on the magnetic field lines.

The floating potential shows this feature more clearly because of the low uncertainty as compared with the other plume properties measured. Inspection of the T_e and n_e data corresponding to these V_f plots suggested that the floating potential decreases drastically because of an increased electron temperature on the cathode side of the division, rather than a sudden drop in plasma potential. Nonetheless, the potential in the cathode region is lower than in the near-field plume, and often bordered by a distinct region of plasma that is lower still in potential, as in Fig. 5. The existence of a double layer conforming to the magnetic field is a clear indication of the importance of the external field of the thruster in cathode coupling processes.

C. Average Near-Field Plume Properties

As a means of studying the trends in the variation of near-field plume plasma properties with cathode position, we have chosen to average the plasma properties in the near-field region to create a scalar value that can be easily compared. This raises the question, "What, exactly, is the near-field region?" Given the trapping effect of the separatrix discussed in the previous section, and the relatively similar properties seen inside the separatrix, we have chosen to define the near-field region as the volume inside a hemi-ellipsoid centered on the origin. The volume is defined by:

$$\left(\frac{r}{63\ \text{mm}}\right)^2 + \left(\frac{z}{70\ \text{mm}}\right)^2 < 1, \qquad z > 0 \tag{28}$$

which approximates the separatrix for the original outer pole. Figure 8 shows the averaging area overlayed on the magnetic field data. The same region is used for the EOP data, thereby maintaining the same number of data points and spatial extent. This was done to enable comparisons between OOP and EOP data. To perform the average, the data points were interpolated onto a 5 mm × 5 mm grid, which is the size of the minimum grid spacing used for these data. The interpolation is a mathematical convenience to handle missing data points. The values at each grid vertex were then weighted by their corresponding cylindrical volume element and the averages and standard deviations computed. For a given property x (T_e, n_e, etc.), the average $\bar{x}$ is computed by

$$z_{\max} = 70\ \text{mm} \tag{29}$$

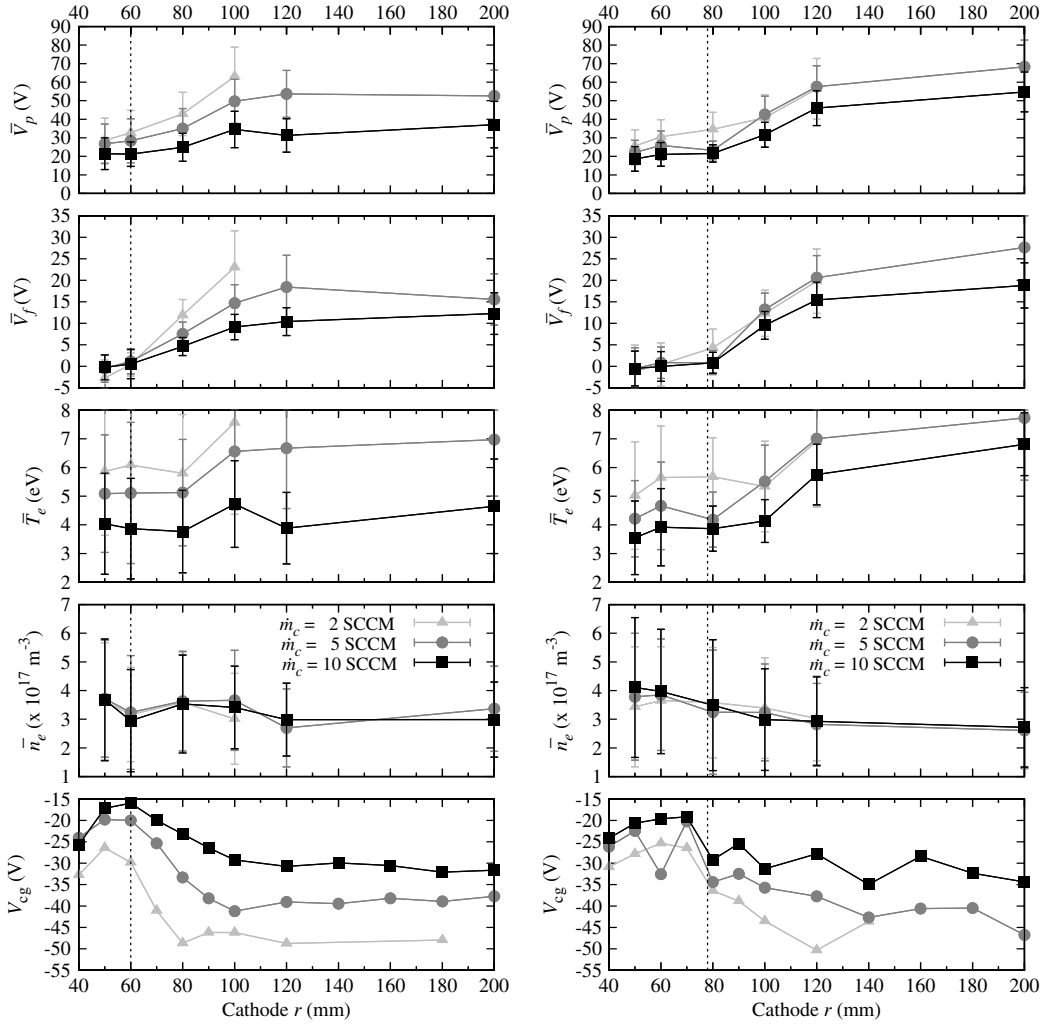

a) OOP **b) EOP**

Fig. 9 Average near-field plume properties as a function of cathode position. Error bars represent standard deviations of the averaged quantities.

$$r_{\max}(z) = 63\ \text{mm}\sqrt{1-\left(\frac{z}{70\ \text{mm}}\right)^2} \tag{30}$$

$$D = \int_0^{z_{\max}} \int_{-r_{\max}}^{r_{\max}} r\,\mathrm{d}r\,\mathrm{d}z \tag{31}$$

$$\bar{x} = \frac{1}{D}\int_0^{z_{\max}} \int_{-r_{\max}}^{r_{\max}} xr\,\mathrm{d}r\,\mathrm{d}z \tag{32}$$

and the standard deviation σ_x is given by

$$\langle x^2\rangle = \frac{1}{D}\int_0^{z_{\max}} \int_{-r_{\max}}^{r_{\max}} x^2 r\,\mathrm{d}r\,\mathrm{d}z \tag{33}$$

$$\sigma_x = \sqrt{\langle x^2\rangle - \bar{x}^2} \tag{34}$$

Figure 9 presents the average plasma potential, floating potential, electron temperature, and electron density for the near-field region. The average provides a convenient way to look at broad trends in the data. Figure 9a shows the data taken with the original outer pole, while Fig. 9b shows the data for the extended outer pole. The dashed line shows the radial location of the separatrix at the cathode axial position of 30 mm. The error bars represent the standard deviation of the averaged points.

Studying Fig. 9, one notices a general upward trend in both potentials and electron temperature as the cathode is moved farther away from the thruster axis and as $\dot{m}_c$ is reduced. This change in potential and V_{cg} is reminiscent of the work on gridded ion thruster performed by Ward and King [20]. Similar changes in potential have also been noted by Smirnov and Raitses while driving the cathode with "extra" heater power [21]. Electron density remains generally flat, perhaps decaying slightly. Note that the plasma potential generally mirrors the cathode coupling potential: as V_{cg} decreases, V_p increases such that the potential difference between the two points increases all the more. Interestingly, a different trend was seen by Hofer et al. [22] and Hofer [23], when working with trim coils. Hofer noted an increase in both floating potential (presumably implying an increase in plasma potential) and V_{cg} rather than opposing trends. In those experiments the cathode was not repositioned. Instead, the magnetic field structure was varied, which may have affected the coupling in a different way than was seen in the present experiments.

The increase in near-field plasma potential is to be expected if the magnetic field is significantly impeding the progress of electrons from the cathode to the beam and anode. Placing the cathode at further radial distances induces a greater impedance, as the electrons must traverse a greater distance across the magnetic field. The potential must increase to compensate for the increased impedance. Most interestingly, the variation of both plasma potential and the cathode coupling voltages with cathode position are relatively flat inside the separatrix, excluding V_{cg} at 40 mm, at which point the cathode physically blocked the exit channel. Only when the cathode is moved outside the separatrix does the near-field plasma potential increase and the cathode coupling voltage decrease significantly. This suggests improved coupling when the cathode is within the separatrix. Phenomenologically, this is reasonable, since electrons bound to magnetic field lines outside the separatrix are directed further downstream and ultimately away from the beam, while those on internal field lines are directed immediately to the beam.

The rate at which the potentials, both V_p and V_{cg}, change with cathode position as the cathode is moved away from the separatrix increases with cathode mass flow rate. This suggests that there is improved mobility due to collisions between electrons and neutrals, that is, an increased classical mobility component, which is to be expected at higher cathode flow rates. This effect has been repeatedly noticed [20,24–27].

The increased near-field plume plasma potential has the effect of increasing ion beam divergence. The correlation between the two can be seen in Fig. 10, which shows the average near-field plume plasma potential (as in Fig. 9) overlaid with the beam divergence efficiencies from Fig. 3. Note that the efficiencies are plotted on a reversed y-axis. The correlation between the two processes is due to the fact that the electric field immediately external to the thruster is largely radial. The greater the potential in the near field, the higher the diverging force on the ions. As an example, Fig. 11 shows the direction of the electric field calculated by taking the gradient of the plasma potential for the 60 and 120 mm cathode positions using the OOP. One notes the generally stronger radial components in the 120 mm case.

The increased external plasma potential may also explain the general trend of the both voltage utilization and velocity distribution efficiencies increasing with increasing cathode position beyond 60 mm. As the near-field plume reaches higher potentials, it is likely that the higher potential regions inside the channel are also pulled further downstream. This gives ions created further downstream greater energy, thus increasing η_V. If the primary ionization region is not drawn down stream as far as the high-potential region, then there would be a corresponding decrease in population of the slower moving ions. That would result in a decreased spread in velocity space, thereby improving η_{vdf}. However, without internal measurements of the HET it is impossible to confirm this speculation.

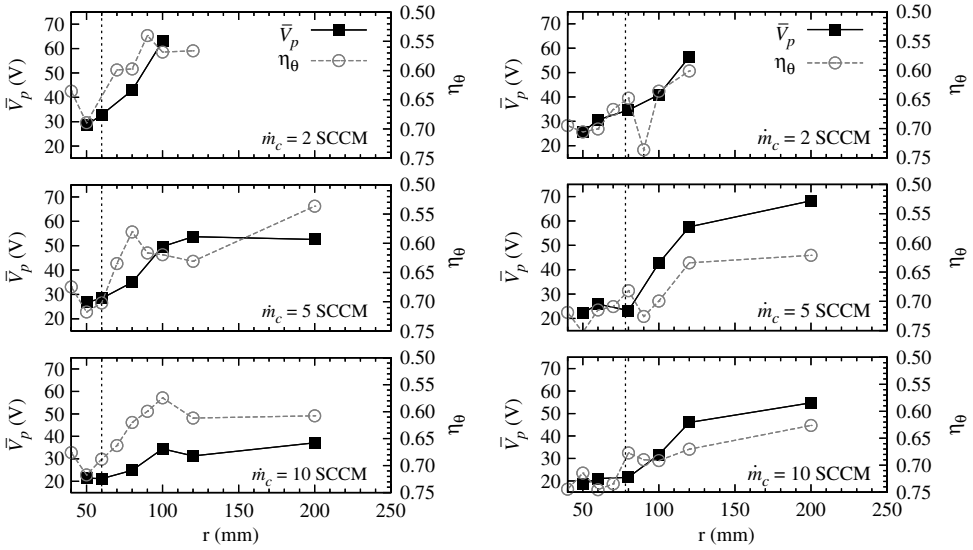

a) Original outer pole **b) Extended outer pole**

Fig. 10 Comparison of the average near-field plasma potential to the beam divergence efficiency.

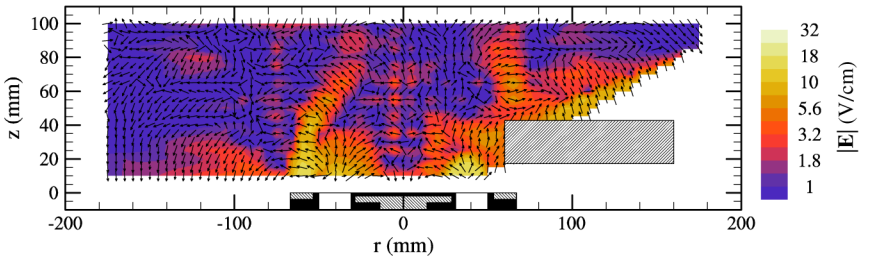

a) Cathode r = 60 mm

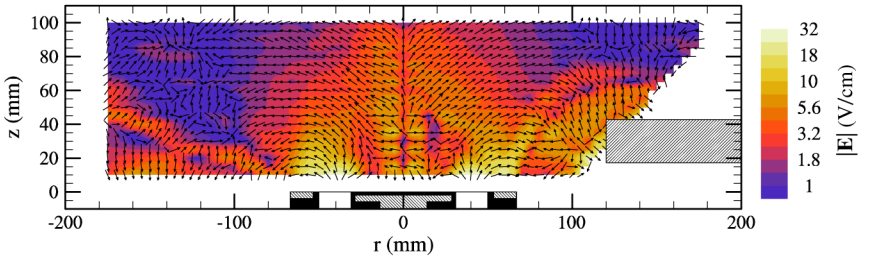

b) Cathode r = 120 mm

Fig. 11 The electric field for $\dot{m}_c = 10$ SCCM with the cathode at 60 and 120 mm on the OOP configuration. The colormap shows field magnitude. The arrows show the direction of the field (in color online).

V. Conclusions

It is clear that the cathode position relative to the magnetic field topology affects the cathode coupling and the performance of the thruster. As the cathode is positioned further from the separatrix such that the cathode electrons must cross through stronger magnetic field lines to reach the ion beam, the plasma of the system must compensate for the increased impedance. It does this by simultaneously lowering the cathode potential and raising the near-field plume potential. This provides stronger electric fields and enable electron transport across the field lines.

However, the plasma thus configured is less efficient at generating thrust. Of course, the decreased cathode coupling voltage leaves less energy available for accelerating ions. More interestingly, the beam divergence increases are due, at least in part, to the increased radial component of the electric field in the near-field plume. The behavior of the other efficiency loss mechanisms is less clear. Changes are certainly seen in current, voltage, and velocity distribution efficiencies. However, the increases in voltage and velocity distribution efficiencies seem to partially offset the decreases in cathode coupling and beam divergence efficiencies as the cathode is positioned further from the thruster. Without internal plasma measurements of the thruster, it is impossible to conclusively say why this happens.

The importance of the separatrix as a dividing line between more and less efficient cathode coupling and thruster operation, for those thrusters that exhibit the feature, is also shown. The line is not a hard boundary. A cathode placed just outside the separatrix does not perform significantly worse than one placed just inside of it. However, the data suggest that as the cathode approaches the separatrix from the outside, the performance improves. This is seen clearly in the cathode coupling and beam divergence efficiency data trends, which exhibit maximums at or just inside the separatrix in both the EOP and the OOP experiments.

While this research has increased our understanding of the effect of cathode position and magnetic field topology on thruster performance, there are still many areas for future exploration. These experiments were conducted with one thruster, one cathode, and only two, very similar, magnetic field topologies. Furthermore, it was done using a nonoptimal propellant, resulting in worse-than-expected performance. While we expect that the work can be generalized to any HET using xenon, this supposition should be confirmed by further experimentation. Also, the effect of the cathode neutral flowfield and, in particular, the cathode angle, has not been studied in detail. Finally, the design of the extended outer pole used in this work was crude. A refined design of the EOP needs to carefully consider the effect of the magnetic circuit on both the internal and external field topologies to more closely match the internal fields while modifying the external.

Acknowledgment

This work was supported by grants from the U.S. Air Force Office of Scientific Research.

References

[1] Sommerville, J. D., and King, L. B., "Hall-Effect Thruster – Cathode Coupling Part I: Efficiency Improvements from an Extended Outer Pole," *Journal of Propulsion and Power*, Vol. 27, No. 4, July 2011, pp. 744–753. doi:10.2514/1.50123

[2] Hofer, R. R., Johnson, L. K., Goebel, D. M., and Fitzgerald, D. J., "Effects of an Internally-Mounted Cathode on Hall Thruster Plume Properties," *42nd AIAA/ASME/SAE/ASEE Joint Propulsion Conference*, AIAA Paper 2006-4482, July 2006.

[3] Jameson, K. K., Goebel, D. M., Hofer, R. R., and Watkins, R. M., "Cathode Coupling in Hall Thrusters," *30th International Electric Propulsion Conference*, IEPC Paper 2007-278, Sept. 2007.

[4] Raitses, Y., Smirnov, A. A., and Fisch, N. J., "Enhanced Performance of Cylindrical Hall Thrusters," *Applied Physics Letters*, Vol. 90, No. 22, May 2007, pp. 221502. doi:10.1063/1.2741413

[5] Sommerville, J. D., "Hall-Effect Thruster—Cathode Coupling: The Effect of Cathode Position and Magnetic Field Topology," Ph.D. Dissertation, Michigan Technological Univ., Houghton, MI, 2009.

[6] Johnson, E. O., and Malter, L., "A Floating Double Probe Method for Measurements in Gas Disharges," *Physical Review*, Vol. 80, No. 1, Oct. 1950, pp. 58–68. doi:10.1103/PhysRev.80.58

[7] Brussaard, G. J. H., van der Steen, M., Carrère, M., van de Sanden, M. C. M., and Schram, D. C., "Langmuir Probe Measurements in an Expanding Magnetized Plasma," *Physical Review E (Statistical Physics, Plasmas, Fluids, and Related Interdisciplinary Topics)*, Vol. 54, No. 2, Aug. 1996, pp. 1906–1911. doi:10.1103/PhysRevE.54.1906

[8] Peterson, E. W., and Talbot, L., "Collisionless Electrostatic Single-Probe and Double-Probe Measurements," *AIAA Journal*, Vol. 8, No. 12, Dec. 1970, pp. 2215–2219. doi:10.2514/3.6089

[9] Brockhaus, A., Borchardt, C., and Engemann, J., "Langmuir Probe Measurements in Commercial Plasma Plants," *Plasma Sources Science and Technology* , Vol. 3, No. 4, Nov. 1994, pp. 539–544.

doi:10.1088/0963-0252/3/4/011
[10] Laframboise, J. G., "Theory of Spherical and Cylindrical Langmuir Probes in a Collisionless, Maxwellian Plasma at Rest," UTIAS Report No. 100, Inst. for Aerospace Studies, 1966.
[11] Hargus, W. A., and Cappelli, M. A., "Laser-Induced Fluorescence Measurements of Velocity Within a Hall Discharge," *Applied Physics B: Lasers and Optics*, Vol. 72, No. 8, June 2001, pp. 961–969.
[12] McMaster-Carr Supply Company, "More About Glass, Ceramics, and Carbon" Material Documentation No. 8477KAC, 2008.
[13] Larson, C. W., Brown, D. L., and Hargus, W. A., "Thrust Efficiency, Energy Efficiency and the Role of VDF in Hall Thruster Performance Analysis," *43rd AIAA/ASME/SAE/ASEE Joint Propulsion Conference*, AIAA2007-5270, July 2007.
[14] Ross, J. L., and King, L. B., "Energy Efficiency in Low Voltage Hall Thrusters," *43rd AIAA/ASME/SAE/ASEE Joint Propulsion Conference*, AIAA Paper 2007-5179, July 2007.
[15] Rovey, J. L., Walker, M. L. R., Gallimore, A. D., and Peterson, P. Y., "Magnetically Filtered Faraday Probe for Measuring the Ion Current Density Profile of a Hall Thruster," *Review of Scientific Instruments*, Vol. 77, No. 1, 2006, p. 013503.
doi:10.1063/1.2149006
[16] Morgan, D., *A Handbook for EMC Testing and Measurement*, Institution of Engineering and Technology, London, 2007, p. 214.
[17] Sibson, R., "A Brief Description of Natural Neighbor Interpolation," *Interpreting Multi-Variate Data*, edited by V. Barnett, Wiley, New York, 1981, pp. 21–36, Ch. 2.
[18] Block, L. P., "A Double Layer Review," *Astrophysics and Space Science*, Vol. 55, No. 1, May 1978, pp. 59–83.
doi:10.1007/BF00642580
[19] Hershkowitz, N., "How Does the Potential Get From A to B in a Plasma?" *IEEE Transactions on Plasma Science*, Vol. 22, No. 1, Feb. 1994, pp. 11–21.
doi:10.1109/27.281545
[20] Ward, J. W., and King, H. J., "Mercury Hollow Cathode Plasma Bridge Neutralizers," *Journal of Spacecraft and Rockets*, Vol. 5, No. 10, Oct. 1968, pp. 1161–1164.
doi:10.2514/3.29442
[21] Smirnov, A. A., and Raitses, Y., "Controlling the Plasma Flow in the Miniaturized Cylindrical Hall Thruster," *IEEE Transactions on Plasma Science*, Vol. 36, No. 5, October 2008, pp. 1998–2003.
doi:10.1109/TPS.2008.2002148
[22] Hofer, R. R., Jankovsky, R. S., and Gallimore, A. D., "High-Specific Impulse Hall Thrusters, Part 1: Influence of Current Density and Magnetic Field," *Journal of Propulsion and Power*, Vol. 22, No. 4, July 2006, pp. 721–731.
doi:10.2514/1.15952
[23] Hofer, R. R., "Development and Characterization of High-Efficiency, High-Specific Impulse Xenon Hall Thrusters," Ph.D. Dissertation, Univ. of Michigan, Ann Arbor, MI, 2003.
[24] Tilley, D. L., de Grys, K. H., and Myers, R. M., "Hall Thruster-Cathode Coupling," *35th AIAA/ASME/SAE/ASEE Joint Propulsion Conference*, AIAA Paper 99-2865, June 1999.
[25] Albarède, L., Lago, V., Lasgorceix, P., Dudeck, M., Burgova, A., and Malik, K., "Interaction of a Hollow Cathode Stream with a Hall Thruster," *28th International Electric Propulsion Conference*, IEPC Paper 03-333, March 2003.
[26] Manzella, D. H., Jankovsky, R. S., and Hofer, R. R., "A Laboratory Model 50 kW Hall Thruster," *38th AIAA/ASME/SAE/ASEE Joint Propulsion Conference*, AIAA Paper 2002-3676, July 2002.
[27] Manzella, D. H., Jacobson, D., and Jankovsky, R. S., "High Voltage SPT Performance," *37th AIAA/ASME/SAE/ASEE Joint Propulsion Conference*, AIAA Paper 2001-3774, July 2001; also NASA TM-2001-21135.

J. Blandino
Associate Editor